3.3 Transition Radiation Detector (TRD)

3.3.1 Design considerations

The main purpose of the ALICE Transition Radiation Detector (TRD) [16] is to provide electron identification in the central barrel for momenta above 1 GeV/c. Below this momentum electrons can be identified via specific energy loss measurement in the TPC. Above 1 GeV/c transition radiation (TR) from electrons passing a radiator can be exploited in concert with the specific energy loss in a suitable gas mixture to obtain the necessary pion rejection capability. In conjunction with data from the ITS and the TPC it is possible to study the production of light and heavy vector-meson resonances and the dilepton continuum both in pp as well as in Pb–Pb collisions. Exploiting the excellent impact parameter resolution of the ITS it is furthermore possible to reconstruct open charm and open beauty in semi-leptonic decays.

The TRD was designed to derive a fast trigger for charged particles with high momentum. It is part of the Level 1 trigger and can significantly enhance the recorded Υ-yields, high-p_{t} J/ψ, the high-mass part of the dilepton continuum as well as jets.

The design parameters of the TRD are the following:

Pion rejection capability This is governed by the signal-to-background ratio in the measurement of J/ψ production and its p_{t} dependence. This led to the design goal for the pion rejection capability of a factor 100 for momenta above 1 GeV in central Pb–Pb collisions/c [6]. The measurement of the lighter vector-mesons and the determination of the continuum between the J/ψ and the Υ will only be feasible when this level of rejection can be reached.

Position and momentum resolution It is crucial to be able to match to the TPC in order to exploit the combined momentum resolution leading to an overall mass resolution of about 100 MeV/c^2 at the Υ-mass (for B = 0.4 T). The required pointing accuracy for electrons needs to be on the level of a fraction of a TPC pad. The anticipated momentum resolution of the TRD of 3.5 (4.7)% at 5 GeV/c (depending on multiplicity) see Table 3.13 will crucially determine the sharpness of the trigger threshold in p_{t} as well as the capability to reject fake tracks.

Radiation length It has to be minimized in order to reduce Bremsstrahlung leading to incorrect momentum determination or loss of electrons and to reduce photon conversions resulting in increased occupancy as well as incorrect matching.

Detector granularity In the bending direction this is governed by the desired momentum resolution and in longitudinal direction by the need to correctly identify and track electrons through all layers of the detector even at the largest anticipated multiplicities. For the desired quality of the reconstructed dilepton pair signal (mostly dictated by the tracking efficiency) this leads to pads with an average area of about 6 cm^2, a tracking efficiency of 90% can thus be achieved for single tracks.
Including secondary particles this leads to a maximum occupancy of 34% at the highest simulated multiplicity density of $\mathrm{dN_{ch}}/\mathrm{d}\eta = 8000$.

3.3.2 Detector layout

The final design of the TRD is depicted in Fig. 3.40. The TRD consists of 540 individual readout detector modules. They are arranged into 18 super modules (right panel of Fig. 3.40) each containing 30 modules arranged in five stacks along z and six layers in radius. In longitudinal (z) direction the active length is 7 m, the overall length of the entire super module is 7.8 m, its total weight is 1650 kg.

Each detector element consists of a carbon fibre laminated Rohacell/polypropylene fibre sandwich radiator of 48 mm thickness, a drift section of 30 mm thickness, and a multi-wire proportional chamber section (7 mm) with pad readout. The pad planes are supported by a honeycomb carbon-fibre sandwich

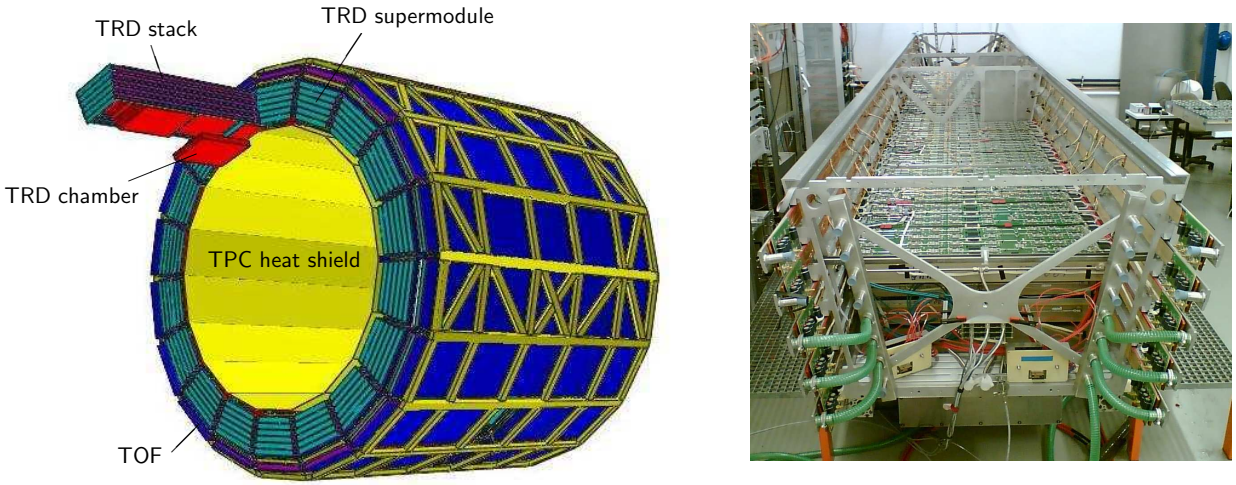

Figure 3.40: Left panel: Schematic drawing of the TRD layout in the ALICE space frame. Shown are 18 super modules each containing 30 readout chambers (red) arranged in five stacks of six layers. One chamber has been displaced for clarity. On the outside the TRD is surrounded by the Time-Of-Flight (TOF) system (dark blue). On the inside the heat shield (yellow) towards the TPC is shown. Right panel: Super module during assembly with the first three layers installed.

back panel (22 mm). While very light, the panel and the radiator provide enough mechanical rigidity of the chamber to cope with overpressure up to 1 mbar to ensure a deformation of less than 1 mm. The entire readout electronics is directly mounted on the back panel of the detector. Including the water cooling system the total thickness of a single detector layer is 125 mm. In the bending plane ($r\varphi$) each pad row consists of 144 pads. The central chambers consist of 12, all others of 16 pad rows. This leads to an overall channel count of 1.18×10^6. The total active area subtended by the pads is 716 m^2. The operating conditions of the detector are summarized in Table 3.13.

Cross-sectional views of one TRD chamber together with average signals are shown in Fig. 3.41. Ionizing radiation produces electrons in the counting gas (Xe/CO_2 (85:15)). Particles exceeding the threshold for transition radiation production ($\gamma\approx1000$) will in addition produce about 1.45 X-ray photons in the energy range of 1 to 30 keV. X-rays in this energy regime are efficiently converted by the high-Z counting gas with the largest conversion probability at the very beginning of the drift region. All electrons from ionization energy loss and X-ray conversions will drift towards the anode wires. After gas amplification in the vicinity of the anode wires the signal is induced on the readout pads. Signals of a typical track are shown in the inset of the central panel of Fig. 3.41. The inclination of the track in the bending direction is a direct measure of its transverse momentum. For particles with a momentum of 2 GeV/c the average amplitude of the cathode pad signal versus drift time is shown in the right panel. Two effects lead to an efficient discrimination between electrons and pions: i) the increased specific energy loss of electrons compared to pions at this momentum (difference between triangles and squares) and ii) the absorption of transition radiation generated by electrons (circles) predominantly at the beginning of the drift section corresponding to large drift times.

3.3.3 TRD performance

As outlined above the performance of the TRD is characterized by its particle identification capability and its tracking performance.

3.3.3.1 Electron identification

The figure of merit for the TRD in terms of electron identification is its power to reject pions at a given electron efficiency (we choose 90%). This is usually expressed in terms of the pion efficiency (we aim at 1%). A parameterization of the measured amplitude spectra as a function of drift time and momentum

Table 3.13: Summary of TRD parameters.

Pseudo-rapidity coverage	$-0.84 < \eta < 0.84$
Azimuthal coverage	360°
Radial position	$2.90 < r < 3.68$ m
Total number of detector modules	540 arranged in 18 super modules
Largest/smallest module	113×145 cm^2 (91×122 cm^2
Active detector area	683 m^2
Radiator	fibre/foam sandwich, 4.8 cm per layer
Radial detector thickness	$X/X_0 = 23.4\%$
Module segmentation	144 in φ 12–16 in z
Typical pad size	0.7×8.8 cm^2
Total number of pads	1.18×10^6
Detector gas	Xe/CO_2 (85%/15%)
Gas volume	27.2 m^3
Depth of drift region	3 cm
Depth of amplification region	0.7 cm
Drift field	0.7 kV/cm
Drift velocity	1.5 cm/μs
Longitudinal/transverse diffusion	$D_L = 250\,\mu m/\sqrt{cm}$ $D_T = 180\,\mu m/\sqrt{cm}$
Lorentz angle	8° at magnetic field 0.4 T
Number of readout channels	1.18×10^6
Time samples in r (drift)	20
ADC	10 bit, 10 MHz
Number of multi-chip modules	70848
Number of readout boards	4104
Pad occupancy for $dN_{ch}/d\eta = 8000$	34%
Pad occupancy in pp	2×10^{-4}
Space-point resolution at 1 GeV/c in $r\varphi$	400(600) μm for $dN_{ch}/d\eta = 2000$ ($dN_{ch}/d\eta = 8000$)
in z	2 mm (offline)
Momentum resolution	$\delta p/p = 2.5\% \oplus 0.5\%(0.8\%)p$/(GeV/$c$) for $dN_{ch}/d\eta = 2000$ ($dN_{ch}/d\eta = 8000$)
Pion suppression at 90% electron efficiency	better than 100 for p = 1 - 6 GeV/c
Event size for $dN_{ch}/d\eta = 8000$	11 MB
Event size for pp	6 kB
Trigger rate limit	100 kHz

both for electrons and pions provides the necessary likelihood distributions [100] that allow to evaluate the electron identification performance.

Specific energy loss Measurements of the specific energy loss of electrons and pions of 2 GeV/c momentum in the Xe/CO_2 gas mixture are shown in Fig. 3.42 along with simulations. A correct understanding of the particle separation capability relies on a precise understanding of the details in the specific energy deposit of electrons and pions. Figure 3.42 demonstrates the level of agreement that has been achieved in the simulations. In that context it has been shown that a correct description of the escape probability of energetic δ-electrons is needed to describe the tails of the energy distributions as well as their momentum dependence [101].

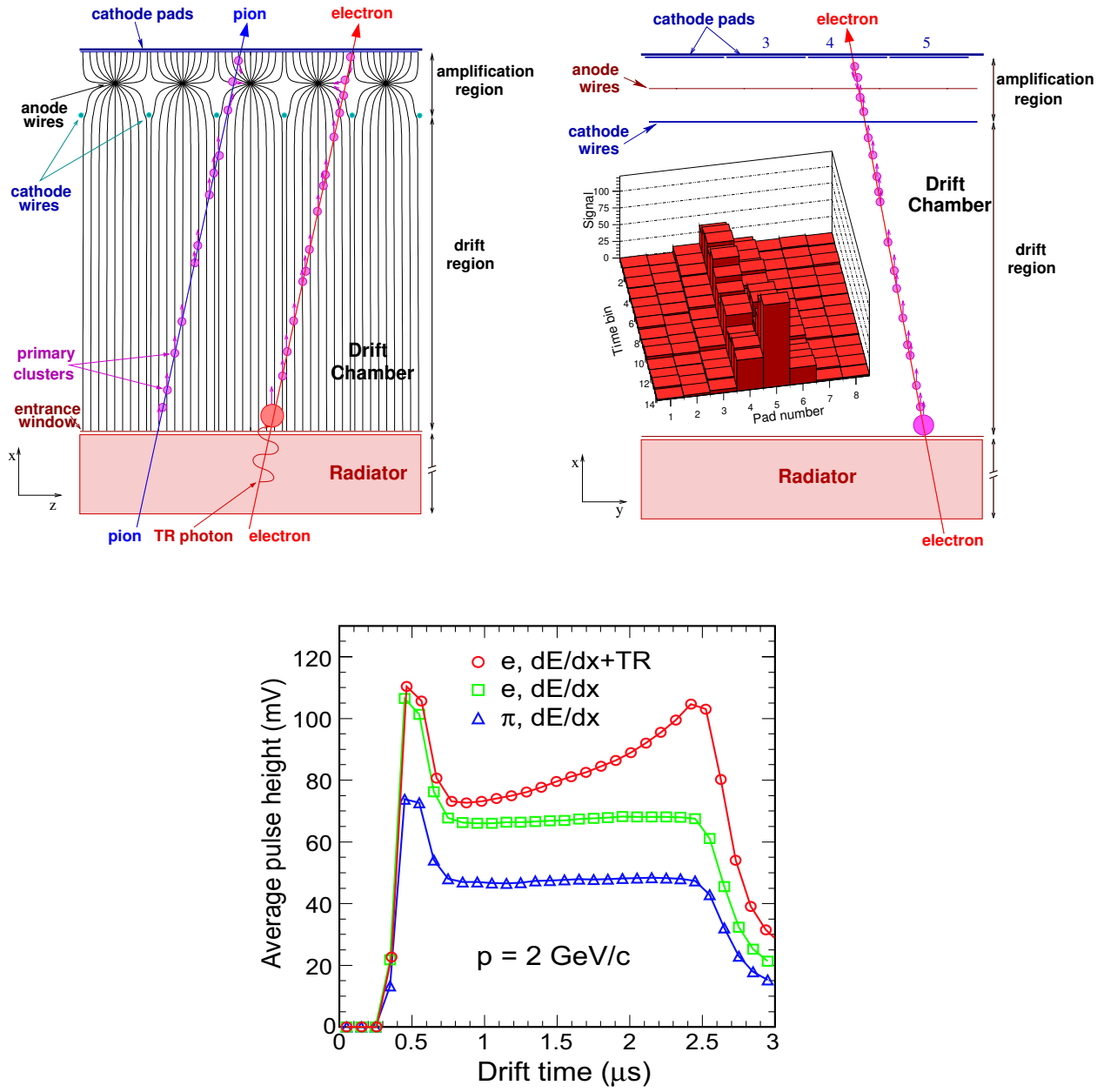

Figure 3.41: Schematic cross-sectional view of a detector module in *rz*-direction (top left panel) and *r*φ-direction (top right panel). The inset shows the charge deposit from an inclined track which is used for momentum reconstruction. The bottom panel shows the average pulse height as a function of drift time for pions (triangles), electrons without a radiator (squares) and electrons with a radiator (circles) for 2 GeV/*c* particles.

Transition radiation The radiator is a composite structure using different inhomogeneous materials. The front and back face consist of 8 mm Rohacell foam covered with 0.1 mm carbon fibre laminate and 25 μm aluminized mylar. It is filled with irregular polypropylene fibre mats (average fibre diameter 20 μm). The transition radiation production of this structure has been evaluated in prototype tests following [103]. The production of transition radiation sets in at an electron momentum of 0.5 GeV/*c* and levels off at about 2 GeV/*c* where on average 1.45 transition radiation photons are produced of which 1.25 are detected per incident electron [102]. The measured transition radiation energy spectra along with simulations are shown in Fig. 3.43.

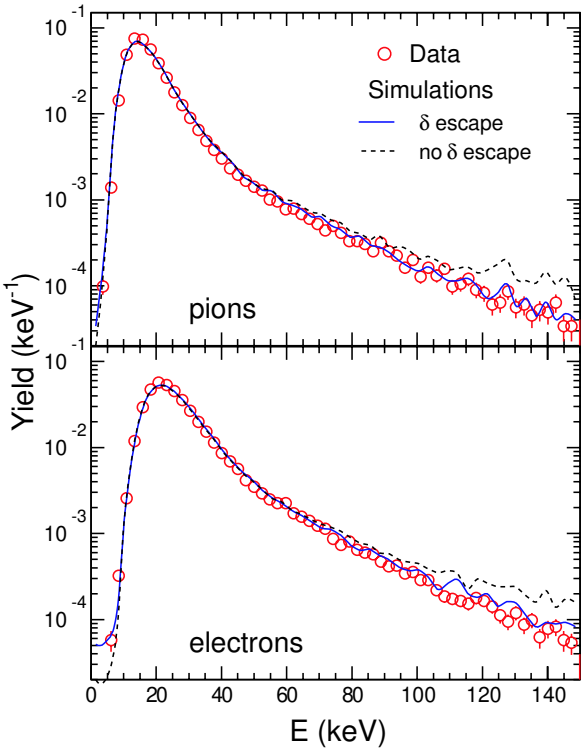

Figure 3.42: Measurement of the specific energy deposit of 2 GeV/c pions (top) and electrons (bottom) in the nominal Xe,CO_2 gas mixture along with simulations [101].

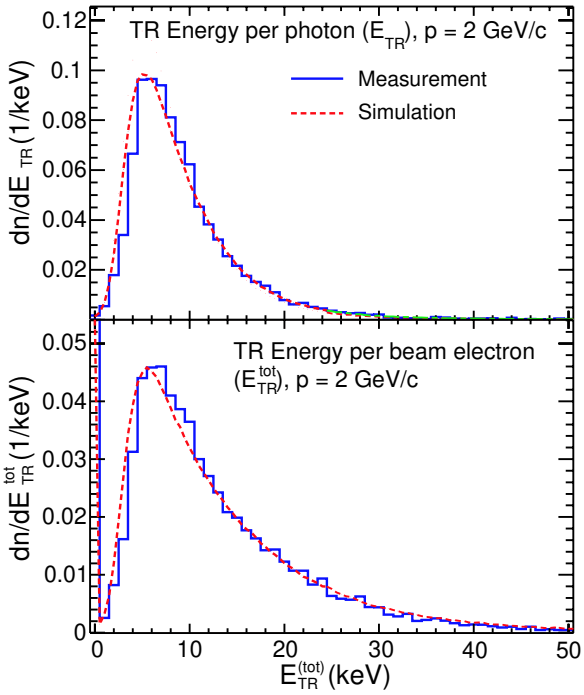

Figure 3.43: Measurement and simulation of the transition radiation spectrum from 2 GeV/c electrons with the ALICE TRD radiator sandwich. The top panel shows the energy distribution of TR photons, the bottom panel the response per incident electron [102].

Pion rejection The resulting pion rejection capability was determined as a function of particle momentum. The results are shown in Fig. 3.44 for two different sets of data. One was obtained using six full-size TRD chambers (big stack), the other are extrapolations of results obtained with smaller prototype chambers (small DCs). Plotted is the percentage of pions erroneously identified as electrons versus momentum at an electron efficiency of 90%. The analysis was based on the likelihood of total deposited charge (L-Q). Along with the measurements, results from simulations are shown applying two-dimensional likelihoods on total deposited charge and position (L-Q1,Q2) as well as analysis based on neural networks (NN) [100]. These methods provide a factor 2–5 increase of the pion rejection capability compared to the simple likelihood analysis on total deposited charge.

3.3.3.2 Tracking

The chief tracking device in ALICE is the TPC. The needed tracking capability of the TRD is derived from the requirement of a reasonably sharp trigger threshold for individual particles in the range of up to $p_t \approx 10$ GeV/c ($\delta p_t/p_t \approx 5\%$ at 5 GeV/c). For particles with large momentum the tracking through the six layers of the TRD improves the overall momentum resolution of the tracking through the central barrel, see Chapter 7.

Position resolution The aforementioned tracking requirements in the nominal magnetic field of 0.5 T, require a position resolution for each time bin of $\sigma_y \lesssim 400\mu$m and a resulting angular resolution per layer of $\sigma_\varphi \lesssim 1^\circ$. The achievable respective resolutions were measured and are a function of the signal-to-noise ratio [104]. They are shown in Fig. 3.45. At a signal-to-noise ratio of about 40 the detector meets the requirements.

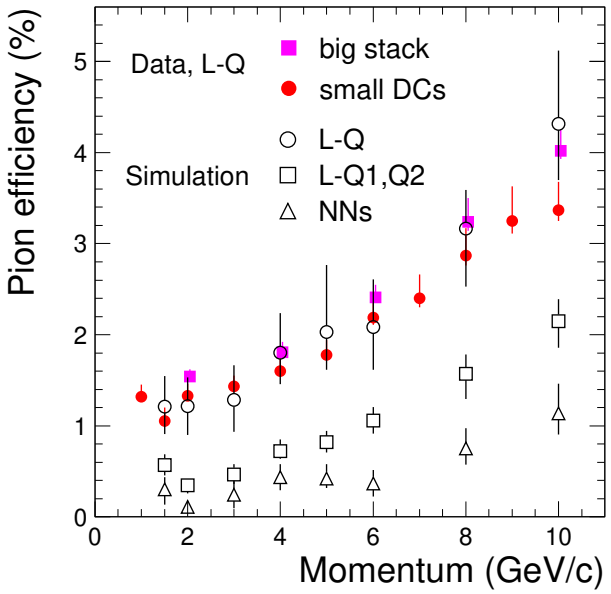

Figure 3.44: Measured pion efficiency as a function of beam momentum applying likelihood on total deposited charge (L-Q) (full symbols) measured with a stack of six chambers and smaller test chambers. Results are compared to simulations (open symbols) for 90% electron efficiency and six layers. These simulations were extended to two-dimensional likelihood on deposited charge and position (L-Q1,Q2) and neural networks (NN) [100].

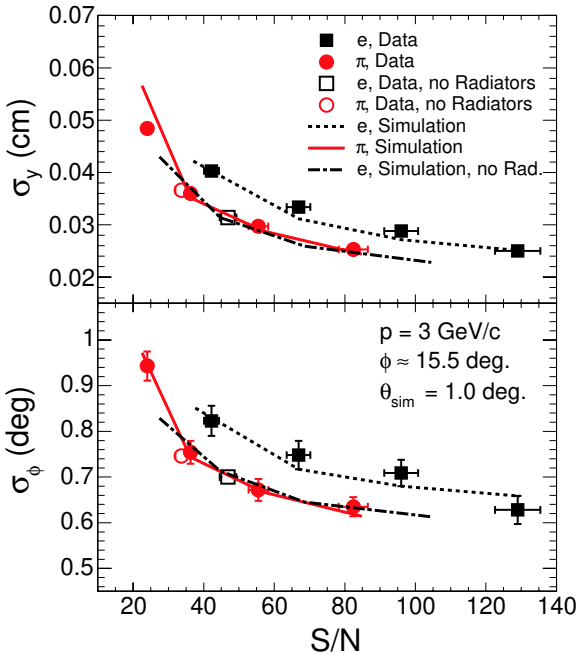

Figure 3.45: Measurements and simulations of the position (top) and angular resolution as a function of the signal-to-noise ratio. Open (full) symbols refer to electrons and pions measured with (without) radiator in front of the drift chamber along with the respective simulations [104].

Momentum resolution Using the above position and angular resolutions the stand-alone tracking resolution of the TRD can be derived for different momenta as a function of multiplicity density. For momenta below 2 GeV/c the stand-alone momentum resolution of the TRD is around $\delta p_t/p_t \approx 2.5-3\%$ with little multiplicity dependence. Through the inclusion of the TRD into the tracking in the central barrel an overall momentum resolution of better than 5% can be obtained up to momenta of about 100 GeV, see Chapter 7.

3.3.4 Readout electronics

3.3.4.1 General layout

An overview of the TRD readout electronics is shown in Fig. 3.46. The electronics, including the optical serializers ORI (two per chamber), is directly mounted on the backside of the detector modules. The data are transmitted to the Global Tracking Unit through 60 optical fibres per super module. The GTU either passes the data directly to the DAQ via the Detector Data Link (DDL) or it further analyzes the data in order to derive a fast Level-1 trigger decision. In that case individual tracklets from different layers of a stack are combined to determine the multiplicity of high-p_t particles or to detect high-momentum e^+e^--pairs. At Level-1 this trigger is transmitted to the Central Trigger Processor (CTP).

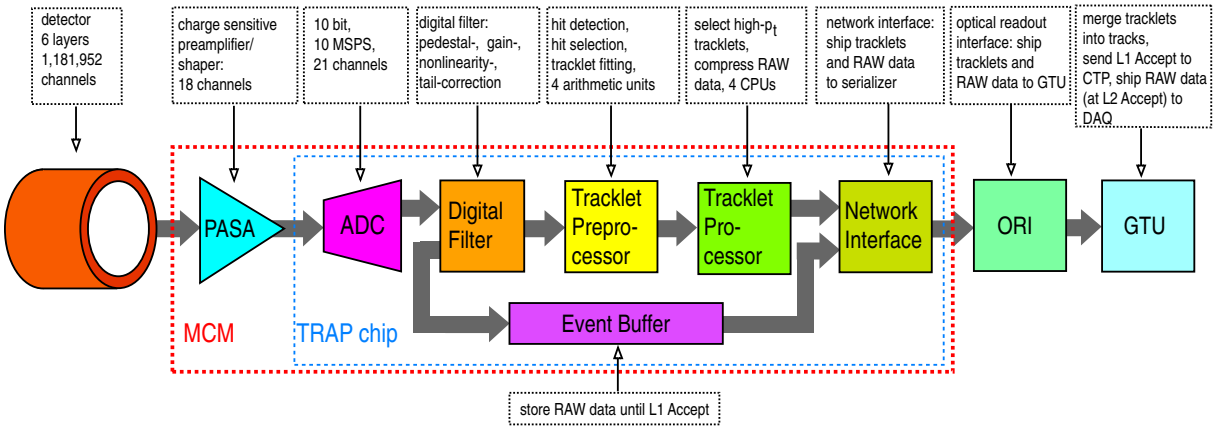

Figure 3.46: Schematic overview of the readout electronics of the TRD.

3.3.4.2 Detector electronics

Most of the on-detector readout electronics are realized as ASICs. Two such chips, an 18-channel full-custom preamplifier shaper (PASA), and a so-called Tracklet Processor (TRAP) were integrated into a multi-chip module (MCM). The PASA [105] is a folded cascode with differential output (120 ns shaping time, 850e ENC for an input capacitance of 25 pF, 12.4 mV/fC gain, and 12 mW/channel power consumption). It was realized using the AMS 0.35 μm CMOS process. Each PASA has 18 input and 21 output channels. For reconstruction of tracklets the extra output channels are fed into the analogue inputs of the TRAPs on neighbouring MCMs to allow for continuous charge sharing across MCM boundaries.

The Tracklet Processor is a mixed signal design realized in the UMC 0.18 μm process. It comprises 21 ADCs, digital filters [106], event buffers, and processing units [107] that allow to calculate the inclination of a track in the bending direction as well as the total charge deposited along the track (Local Tracking Unit - LTU). This feature allows to identify high-p_t particles at the trigger level. Evaluation of the deposited energy will furthermore allow to tag possible electron candidates at the trigger level.

3.3.4.3 Global Tracking Unit (GTU)

After preprocessing of the analogue signals as described above, the resulting track segments from the different detector layers have to be matched in three dimensions for transverse momentum reconstruction. Based on the data of all 1.2 million analogue channels, the reconstruction has to be performed within 6.1 μs to derive the Level-1 trigger decision. The entire trigger timing sequence involving the LTU and the GTU is depicted in Fig. 3.47.

The massively parallel hardware architecture of the GTU is capable of processing up to 20 000 track segments within 2 μs. The core of the GTU, along with a custom bus system, is the so-called Track Matching Unit (TMU). It is an FPGA-based system utilizing PCI and 12 fibre-optical SFP transceiver interfaces gathering the data from a stack of six chambers. It is realized as a CompactPCI plug-in card. The main FPGA is a Xilinx Virtex-4 FX chip which includes an integrated multi-gigabit serializer/deserializer and PowerPC processor blocks.

3.3.4.4 Detector Control System (DCS)

The entire configuration, monitoring, and control of the detector electronics is realized on a single DCS board with an autonomous power supply. There is one DCS board per chamber. The boards comprise an Altera FPGA with ARM9 core, flash memory, Ethernet-, JTAG-, and I^2C-interfaces, 8 analogue and 8 digital inputs as well as 8 digital outputs.

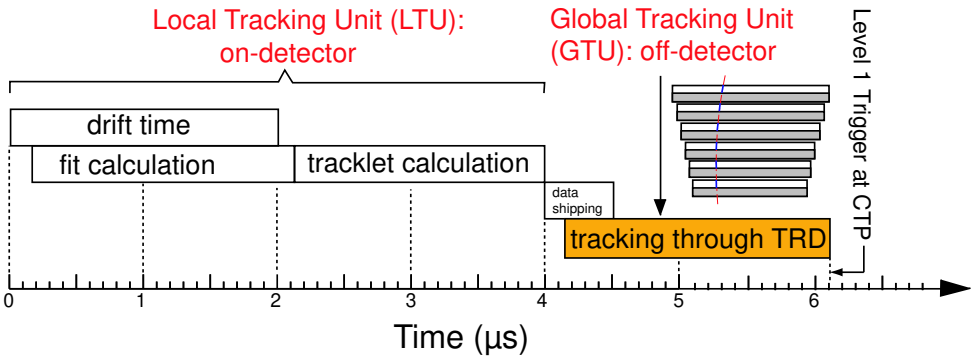

Figure 3.47: Trigger timing diagram for the generation of a high-p_t trigger.

The board reshapes and distributes the central clock signal received via an on-board Trigger Timing Controller (TTC) to all MCMs on the detector. All internal clocks of the MCMs are derived from this central clock. The configuration of different filter and gain parameters as well as zero suppression conditions used for the reconstruction of the tracklets within the Local Tracking Unit (LTU) are handled by the DCS board. It also monitors the temperatures and currents of all individual MCMs. Through its external control lines it is able to shutdown voltage regulators in case of over-temperature or over-current. Moreover, the DCS board can reroute the so-called Slow Control Serial Network in the configuration chain which allows us to bypass faulty MCMs without loss of data from entire readout boards.

The states of all services (low voltage, high voltage, gas, cooling) as well as all states generated or monitored by the DCS board are implemented as Finite-State Machines (FSM) which are operated and controlled via PVSS.

3.4 Time-Of-Flight (TOF) detector

3.4.1 Design considerations

The Time-Of-Flight (TOF) detector [15] is a large area array that covers the central pseudo-rapidity region ($|\eta| \lesssim 0.9$) for Particle IDentification (PID) in the intermediate momentum range, below about 2.5 GeV/c for pions and kaons, up to 4 GeV/c for protons, with a π/K and K/p separation better than 3σ [21, 108]. The TOF, coupled with the ITS and TPC for track and vertex reconstruction and for dE/dx measurements in the low-momentum range (up to about 1 GeV/c), will provide event-by-event identification of large samples of pions, kaons, and protons. In addition, at the inclusive level, identified kaons will allow invariant mass studies, in particular the detection of open heavy-flavoured states and vector-meson resonances such as the ϕ meson. Details on the physics observables that can be addressed and the expected performance are detailed in [4, 21, 108, 109] and in Section 7 of this document.

A large-coverage TOF detector, operating efficiently, with an excellent intrinsic response and an overall occupancy not exceeding the 10–15% level at the highest predicted charged-particle density of dN/dη = 8000 was required; see [21]. This led to the current design with more than 10^5 independent TOF channels. Since a large area had to be covered, a gaseous detector was chosen. In the framework of the LAA project at CERN an intensive R&D programme has shown that the best solution for the TOF detector was the Multi-gap Resistive-Plate Chamber (MRPC) [110, 111].

The key aspect of these chambers is that the electric field is high and uniform over the full sensitive gaseous volume of the detector. Any ionisation produced by a traversing charged particle immediately starts a gas avalanche process which generates the observed signals on the pick-up electrodes. Unlike other types of gaseous detectors, there is no drift time associated with the movement of the electrons to a region of high electric field. Thus the time jitter of these devices is caused by the fluctuations in the growth of the avalanche.